Broadband highly amplified ultrasound in antiresonant hollow core fibers for optoacoustic sensing and neurostimulation

R. E. da Silva[1,2*], D. J. Webb[2], C. M. B. Cordeiro[3], M. A. R. Franco[1]

[1]Institute for Advanced Studies (IEAv), Department of Aerospace Science and Technology
São José dos Campos, 12228-001, Brazil

[2]Aston Institute of Photonic Technologies (AIPT), Aston University
Birmingham, B4 7ET, UK

[3]Institute of Physics Gleb Wataghin, University of Campinas (UNICAMP)
Campinas, 13083-859, Brazil

*E-mail: r.da-silva@aston.ac.uk

Keywords: *antiresonant hollow core optical fibers, high frequency ultrasonic devices, optoacoustic fiber sensors, optoacoustic fiber neurostimulation.*

High frequency broadband ultrasound in nested antiresonant hollow core fibers (NANFs) is investigated for the first time. NANFs have remarkable features to enable high resolution microscale optoacoustic imaging sensors and neurostimulators. Solid optical fibers have been successfully employed to measure and generate ultrasonic signals, however they face issues around attenuation, limited frequency range, bandwidth, and spatial resolution. Here, we numerically demonstrate highly efficient ultrasonic propagation in NANFs from 10 to 100 MHz. The induced pressures and sensing responsivity are evaluated in detail, and important parameters for the development of ultrasonic devices are reviewed. High pressures (up to 234 MPa) and sensing responsivities (up to -207 dB) are tuned over 90 MHz range by changing the diameters of two distinct NANF geometries. To the best of our knowledge, this is widest bandwidth reported using similar diameter fibers. The results are a significant advance for fiber-based ultrasonic sensors and transmitters, contributing to improve their efficiency and microscale spatial resolution to detect, diagnose and treat diseases in biomedical applications.

1. Introduction

Optical fibers offer unique features for biomedical diagnosis and imaging of vessels, tissues, and vital human organs and, more recently, neurostimulation to treat depression, Alzheimer, and other dementias [1–5]. Optoacoustic fiber sensors provide significant sensitivities while reducing the device size compared to the traditional piezoelectric transducers (PZT) [1]. The biological tissues are heated by a pulsed laser generating ultrasonic signals by thermoelastic effect [1]. The ultrasonic waves are coupled in the fiber by fluids in the tissue or ultrasound gel purposely inserted to reduce attenuation [2]. The coupled ultrasound changes the phase of the guided optical modes, which is demodulated by using interferometers [2,6,7]. Fiber sensors employing single mode fibers (SMFs) and Bragg gratings offer effectively short sensing lengths (270 - 350 μm) [2]. However, SMF-based devices detect signals mostly in narrowband resonances, limiting the frequency-dependent axial spatial resolution ($R \sim 1/f$). Increasing frequency (e.g., $f = 25$ - 125 MHz) is required to detect microscale details ($R = 50$ - 10 μm) [1].

Fiber optoacoustic transmitters for brain neurostimulation share similar operation principles and challenges of the sensors. In transmitters, a pulsed laser excites an optical absorber usually composed of carbon nanotubes (CNT) deposited at the fiber tip [8]. The axially generated ultrasonic waves are focused on a microcellular region to activate groups or individual neurons [3–5]. Thus, the fiber tip coupled to the tissue stimulates a very small target region, providing superior spatial resolution compared to PZTs (39.6 μm resolution is achieved using a tapered fiber [4]). In this case, high frequencies favor the propagation of plane acoustic waves, confining the beam to reach the target [3,4]. Nevertheless, the generated acoustic pressures should be sufficiently high (3 to 21.5 MPa) [4,8] to reach the target under strong tissue attenuation (0.6 - 1 dB cm^{-1} MHz^{-1} [1,3]). In this sense, high amplitude ultrasound in the optical fiber over a broad frequency range is therefore demanded to detect or generate acoustic signals with proper spatial resolution. In general, solid fibers provide a maximum frequency and bandwidth of 50 MHz [4].

In this paper, we demonstrate remarkable confinement and amplification of ultrasound in nested antiresonant hollow core fibers (NANFs) from 10 to 100 MHz (corresponding the mesoscopic range of practical sensors [1]). Two state-of-art NANFs with distinct geometries are modeled by using the 3D finite element method (FEM). The theoretical background to compute the NANFs sensing responsivity is presented in Section 2. The tuning of induced pressures and axial strains with fiber diameter is discussed in Section 3.1. The NANFs responsivities and bandwidths are analyzed in Section 3.2. Finaly, Section 3.3 shows the main achievements to increase the interaction of ultrasound and optical waves, indicating promising NANFs geometries specifically for optoacoustic sensing and neurostimulation.

2. Theoretical background

Analytical, semi-analytical and numerical methods have been extensively used to model ideal SMFs, showing their ultrasonic frequency spectrum composed of resonances with peaks at 29 and 70 MHz [9–11]. In general, the range between these resonances from 40 to 60 MHz (and at higher frequencies) is limited by unacceptably high ultrasound attenuation [9–12].

Considering proper ultrasonic propagation in a solid optical fiber, the acoustically induced strains modulate the fiber core refractive index n and fiber length L, inducing an optical phase shift of the guided optical modes as, $\varphi = 2\pi n_{eff} L/\lambda$, where λ is the optical wavelength [2,6,7,10,13]. The phase sensitivity, $S = d\varphi/dP$, is therefore defined by the φ change to the effective acoustic pressure P in the fiber core. Thus, the NR responsivity of an SMF is given by [14],

$$NR = \frac{d\varphi}{\varphi dP} = \frac{1}{dP}\left[\varepsilon_z - \frac{n^2}{2}\left((p_{11} + p_{12})\varepsilon_r + p_{12}\varepsilon_z\right)\right], \quad (1)$$

where, ε_z and ε_r are respectively the axial and radial strains, and p_{11} and p_{12} are the coefficients of the elasto-optic tensor [14]. Phase modulation in hollow core fibers (HCFs) follows similar principles as in SMFs. However, the contributions to *NR* are different as [14–17]

$$NR = \frac{d\varphi}{\varphi dP} = \frac{\varepsilon_z}{dP} + \frac{1}{n_{eff}}\frac{dn_{eff}}{dP}, \quad (2)$$

where, n_{eff} is the effective index of the fundamental optical mode. In contrast to SMFs, the elasto-optic effect in HCFs is negligible since no strains exist inside the air core [15]. In addition, n_{eff} changes caused by induced fiber geometric variations are insignificant compared to length changes [16,17]. As a result, *NR* in (2) is mainly determined by the axial strain ($\varepsilon_z = \Delta L/L$) and the pressure in the HCF as, $NR = \varepsilon_z/dP$ [15] (which is usually presented in dB (20Log (*NR*) [16,17]). Previous studies show that photonic bandgap (PBG) HCFs provide *NR*s (-344 to -310 dB) up to 60x higher than in SMFs at low frequencies (40 Hz - 50 kHz) [14,15]. The increased *NR* is attributed to the reduced silica content (or large air filling fraction) in PBG-HCFs increasing the axial strain. Thus, we have previously demonstrated that suspended core fibers and antiresonant hollow core fibers offer significantly higher ultrasound amplification compared to solid fibers [18–20]. Here, we demonstrate that high frequency acoustic waves are significantly enhanced and confined in NANFs, inducing higher pressures and axial strains even compared to PBG-HCFs. The NANFs dimensions and modeling methods are described in Section 5.

3. Results and discussion

3.1. Ultrasonically induced pressure and axial strain in NANFs

Figure 1 shows the 2D simulation of the power distribution of the fundamental optical mode in properly selected NANFs with an arbitrary diameter *D*. These fibers are composed of a ring of large silica tubes forming the air core and nested silica tubes reducing the confinement losses [21]. Note that the fibers have distinct structures and tubular dimensions, which are designed to provide low loss single mode operation over a broad wavelength range (λ = 600 - 1100 nm) [21]. For the same diameter *D*, NANF A has reduced silica content compared to NANF B (with thinner tubes). Thus, decreasing *D* reduces only the silica jacket modifying ultrasonic properties while keeping unaltered the tubular structure and single mode guidance in the air core.

Figure 2a,b shows the 3D FEM simulation of the induced pressure *P* in the NANFs tubes from *f* = 10 to 100 MHz (for simplicity, only the minimum, medium and maximum *D* are shown). Note that NANFs provide high pressures over the whole ultrasound spectrum. In general, *P* increases with decreasing *D*, shifting, and widening the resonance bands at higher frequencies.

The axially induced strains increase with decreasing *D*, as shown in Figure 2c,d. Broadband resonances from 40 to 100 MHz indicate considerably higher strain magnitudes and bandwidths compared to SMFs [7,11]. NANFs responsivity *NR* is further computed from the induced pressures and strains, as discussed in the next section.

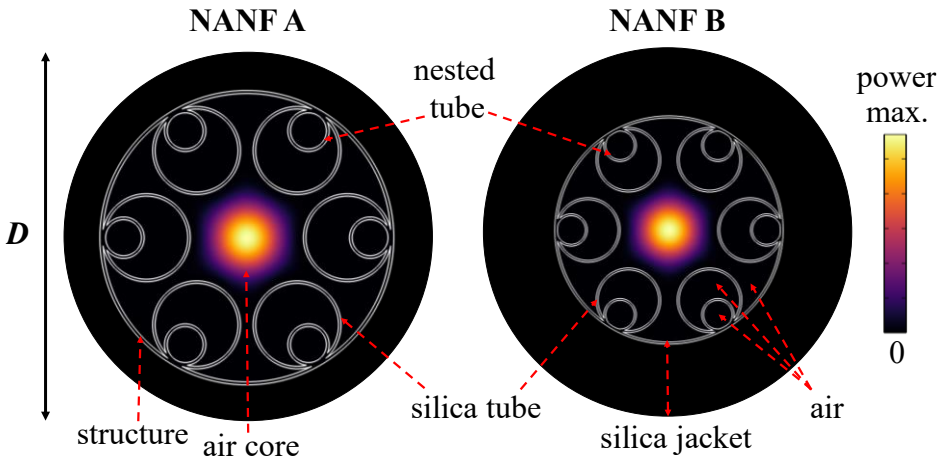

Figure 1. 2D FEM simulation of the power distribution of the fundamental optical mode in the nested antiresonant hollow core fibers (NANFs) with an arbitrary diameter *D*, indicating the geometric structure and material. The modeled NANF A and B geometries are based in the experimental fibers described in [21].

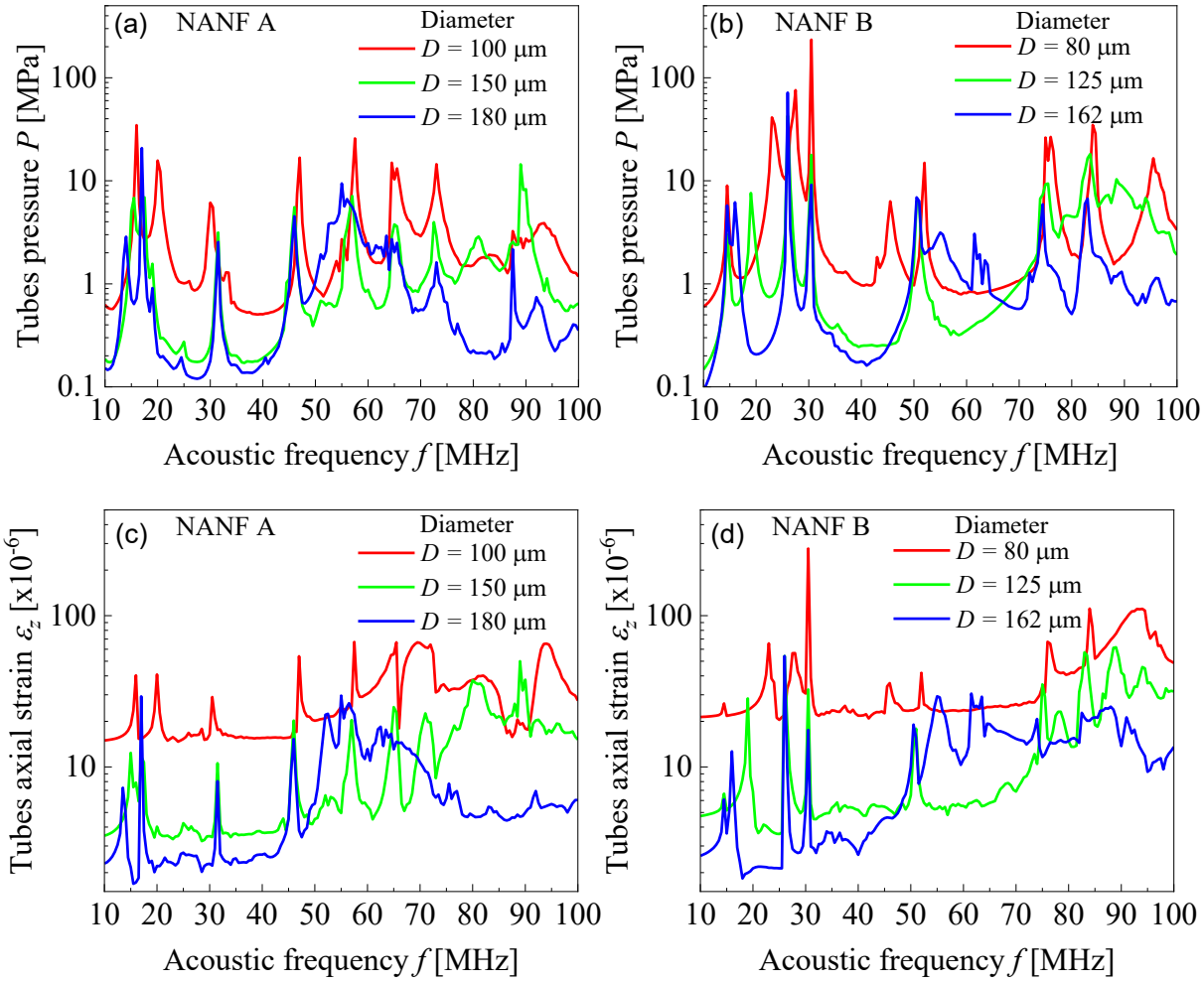

Figure 2. (a) 3D FEM simulation of the ultrasonically induced (a)(b) pressure *P* and, (c)(d) axial strain ε_z in the silica tubes in NANF A and B for selected diameters *D* in the frequency range of *f* = 10 - 100 MHz.

3.2. NANFs responsivity to broadband high frequency ultrasound

Figure 3a,b shows the NANFs responsivity *NR* spectrogram (top view magnitude in terms of frequency and fiber diameter). In general, reducing *D* increases *NR*, as indicated with dark red regions in Figure 3a,b. The dashed black lines indicate relevant bands broadening *NR* for each *D*. Figure 3c,d indicates gaps of lower *NR* between resonances. Note the differences in *NR* magnitude, bandwidth, and frequency caused by the distinct fiber geometries and diameters. Thus, NANF geometries and *D* can be selected to improve ranges of low responsivity (e.g., NANF B - *NR* gap at 25 MHz might be covered by NANF A).

The parameters *P*, ε_z, and *NR* are averaged over $f = 10$ - 100 MHz to provide a figure of merit to compare NANFs with distinct diameters. The effective bandwidth *W* is estimated by totaling the 3-dB bandwidths of resonances with peak magnitude higher than the average spectrum. Figure 4 shows the variation of *P*, ε_z, and *NR*, and their respective effective bandwidths with increasing *D*.

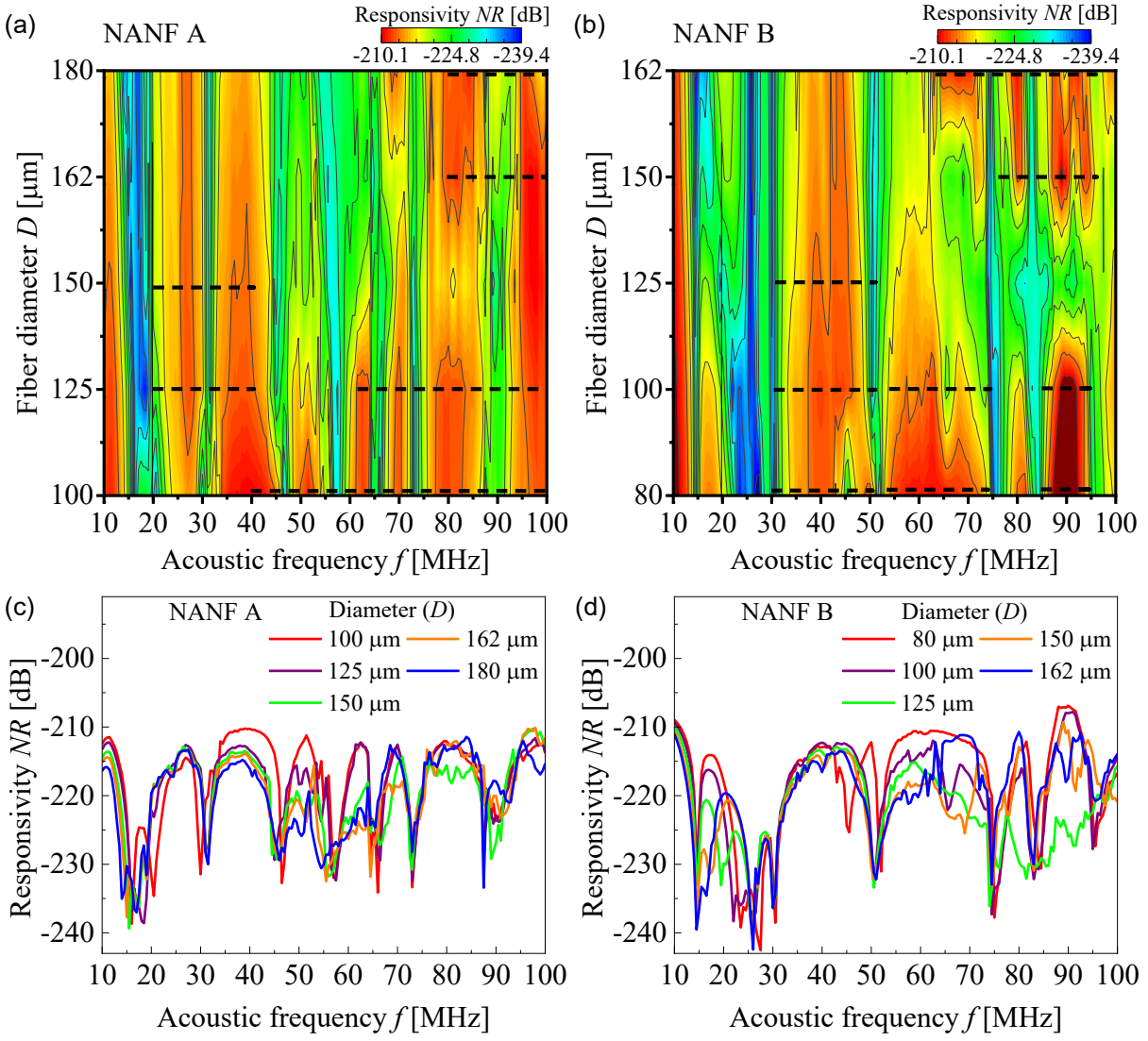

Figure 3. 3D FEM simulation of the responsivity to ultrasonic pressure *NR* in NANF A and B with changing diameter *D* from $f = 10$ to 100 MHz: (a)(b) 2D *NR* spectrograms and, (c)(d) *NR* for the considered fiber diameters.

Figure 4a,c shows increasing P and ε_z by reducing D in both NANFs (NANF B provides higher P for similar diameters probably due to its thinner tubes). Note that most curves in Figure 4 (mainly bandwidths) show magnitude oscillations deviating from a smooth response, indicating resonances of acoustic periods matching with the fiber cross section (as explained in detail in [11]).

NANF A shows wider bandwidths and nearly smooth responses, suggesting that the reduced silica jacket might decrease resonant effects with D. Thus, NANF B is more susceptible to cladding resonances as those observed in SMFs [15,20]. Overall, increasing diameters from 150 µm expanding the silica jacket indicate decreasing effect of the NANFs tubular structure.

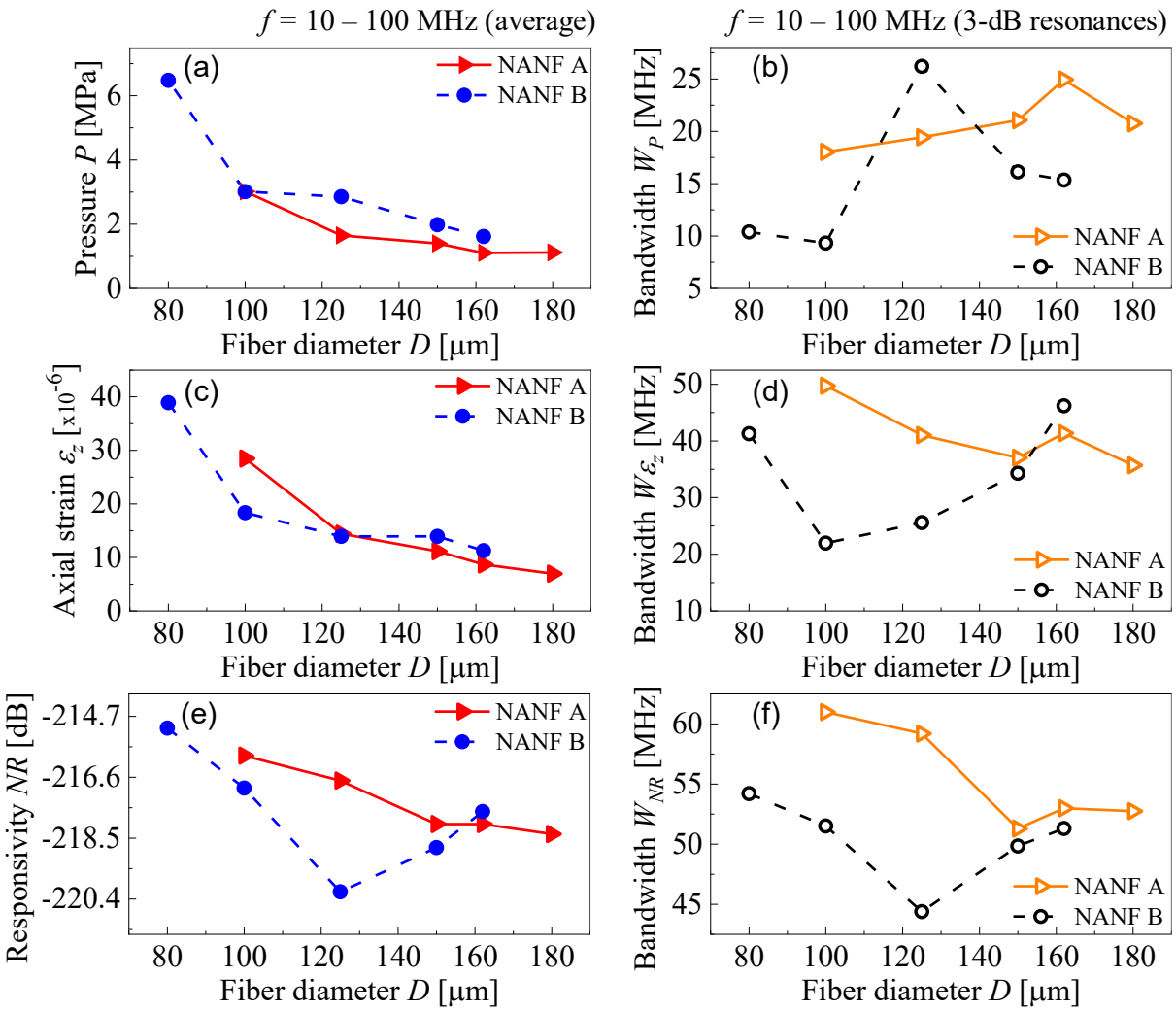

Figure 4. (a)(c)(e) NANFs induced pressure P, axial strain ε_z and responsivity NR with increasing fiber diameter D averaged over f = 10 - 100 MHz. (b)(d)(f) Respective effective bandwidths W for each parameter.

Figure 5a,b shows the frequency response for optimized NANFs diameters with better compromise between high pressure or responsivity, and wide bandwidth. The constant applied stress in the NANFs is equivalent to that inducing P = 0.5 MPa in an SMF (dashed white line in Figure 5a). These simulated P magnitudes are typically higher (up to ~10x) or comparable with those experimentally measured in a solid fiber [8]. In addition, the minimum NR = -220 dB over the whole spectrum (white line) is significantly increased from that in PBG-HCFs (at least 100x higher [14,15]). Table 1 summarizes the NANFs geometries and diameters showing better performances of the evaluated fiber diameters. Overall, this study considers ideal optical fibers, and the achieved ultrasonic performances (magnitudes and bandwidths) might change

with fiber's geometric deviations during the fabrication or mechanical perturbations when in use (e.g., pressing or bending the fibers). Consequently, combination of NANFs with other components or devices might affect the predicted ideal resonances (e.g., damping induced by external agents, absorber, interferometer, coatings).

Figure 6 shows the simulated ultrasound (displacements) in the NANFs with resonances indicated in Figure 5b. Note that the ultrasonic waves propagate mostly in the tubes inducing maximum displacements in the internal tubular edges forming the air core (dark red). Similarly, maximum pressures and strains are also induced at the core edges showing distinct distributions in the tubes depending on the fiber geometry and resonant frequency.

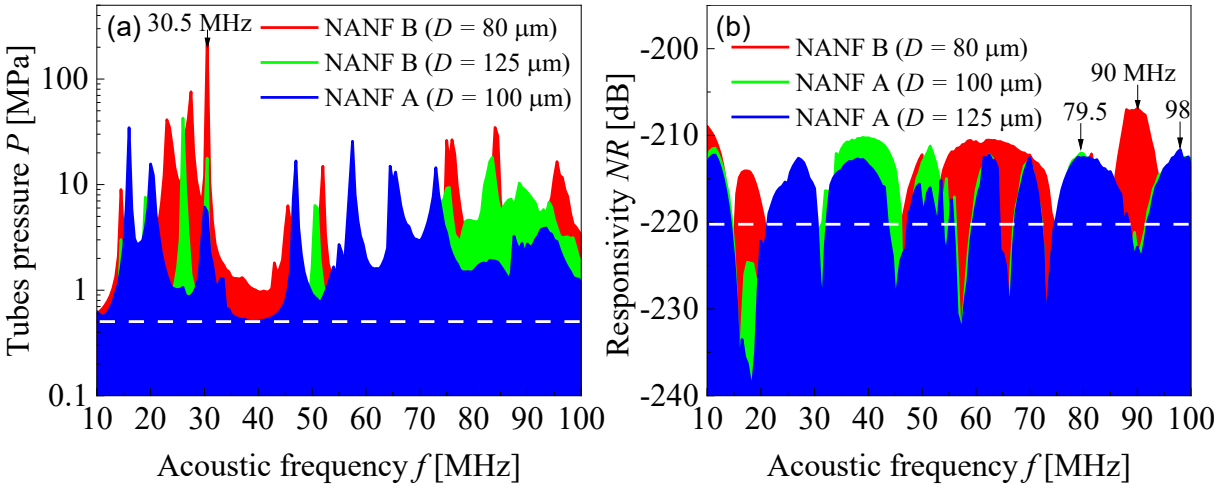

Figure 5. NANFs (a) pressure *P* and (b) responsivity *NR* frequency response indicating the structures (NANF A and B) and fiber diameters *D* suitable for optoacoustic fiber transmitters and fiber sensors (dashed white lines in (a) and (b) indicate respectively, an equivalent input pressure of *P* = 0.5 MPa in an SMF, and the minimum *NR* covered by the selected NANFs over the whole frequency range of *f* = 10 – 100 MHz.

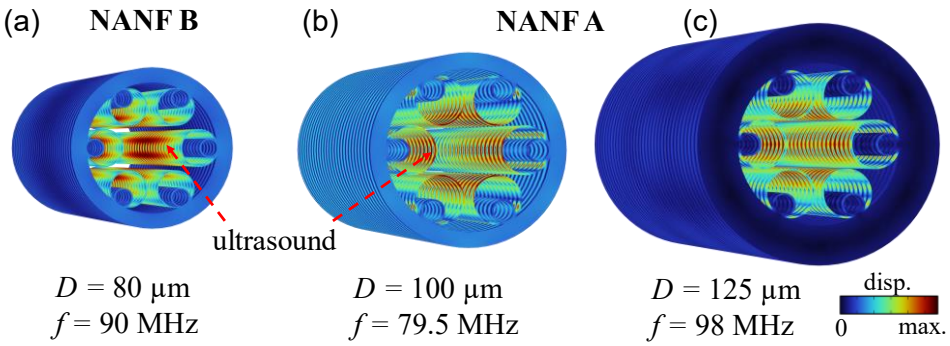

Figure 6. 3D FEM simulation of the high frequency ultrasonic waves (displacements) in (a) NANF B and (b)(c) NANF A with the diameters and resonances indicated in Figure 5b.

Table1. NANFs geometries with promissing performances to generate and sense ultrasound.

	NANF A		NANF B	
Fiber diameter (µm)	100	125	80	125
P peak (MPa)	36	25	234	18
P average (MPa)	3	1.7	6.5	2.8
NR peak (dB)	-210	-212	-207	-210
NR average (dB)	-216	-217	-215	-220
W_{NR} effective 3-dB (MHz)	61	59	54	44
Suitable *P* ranges (MHz)	15-35, 45-75		10-30, 75-100	
Suitable *NR* ranges (MHz)	25-100		10-20, 35-90	10-15, 35-70

P and *NR* are averaged over *f* = 10 - 100 MHz (*P*: pressure, *NR*: responsivity, W_{NR}: bandwidth).

3.3. Outlook considerations for application of NANFs in high frequency ultrasonic devices

We conclude from this study that three important factors contribute to amplify high frequency ultrasound in NANFs in comparison to other optical fibers:

1) NANFs considerably reduce the silica over the fiber cross section since the optical guidance is defined by a few nano tubes. For NANFs with similar air filling fractions, reduced diameter and thinner tubes might provide higher ultrasonic magnitudes (e.g., pressures and strains).
2) The tubular lattice provides an extra degree of freedom in comparison to other hollow core fibers, such as PBG-HCF. The NANF tubes are slightly suspended on the silica jacket, providing high ultrasound amplification.
3) NANFs geometry offers unique properties to confine acoustic waves with periods smaller than fiber diameter (resonances). As a result, broadband resonant waves are tuned by changing the tubular dimensions or *D*, allowing even large diameter fibers amplify ultrasound in the tubes (Figure 6c).

In summary, NANFs might provide extra contributions for fiber-based biomedical devices, in particular:

Optoacoustic fiber sensors:

- NANFs might offer flatter high *NR* over a broad frequency range (90 MHz), which is ideally impossible with solid fibers at the considered frequencies, enabling the observation of microscale details by increasing the spatial resolution.
- NANFs might deliver laser light at the biological samples while collecting the optically generated ultrasound (e.g., by adding a thin transparent mirror at the fiber end, the fiber could be used in combination with Michelson interferometers [15,22]).
- The large diameter NANFs provide better protection and mechanical stability compared to tapered and etched fibers which might expose the optical properties to unwanted changes caused by the external medium.

Optoacoustic fiber transmitters:

- NANFs might provide high ultrasonic pressures over wide bandwidths (90 MHz). The increased *P* contributes to overcome elevated attenuation in biological tissues and optical absorbers, enabling to reach samples at long distances. It might relieve the power and efficiency thresholds of optical absorbers to generate ultrasound.
- The tubular resonances and achieved high frequencies would contribute to generate highly confined ultrasonic beams, increasing the spatial resolution to reach the target even employing NANFs with larger diameters.
- NANFs might reduce unsuitable thermo-induced effects in the biological tissues caused by heating from the laser or absorber [5]. Thus, CNTs could be deposited inside the NANF air core providing large overlap with the laser power, improving the optoacoustic efficiency. Additionally, the ultrasound will be coupled directly from the CNT to the tubes inducing higher acoustic amplitudes in the fiber, which also increases the overall device efficiency.

4. Conclusion

We have numerically demonstrated broadband high frequency ultrasonic waves in antiresonant hollow core fibers for the first time. Two distinct NANF geometries are modeled by using 3D FEM, and the influence of the fiber tubular structure on induced pressures, axial strains and sensing responsivities are evaluated by changing the fiber diameter.

The results show significant ultrasound amplification from 10 to 100 MHz (90 MHz range) to the best of our knowledge, the widest bandwidth reported using similar diameter fibers. In

general, the ultrasonic parameters are amplified by reducing the diameter, which decreases the silica content enhancing resonances in the tubular structure. Consequently, significantly increased bandwidths are achieved. Further advance might consider antiresonant fibers with distinct fiber geometries and tubular dimensions.

NANF B (with D = 80 μm) provides higher magnitudes (P = 234 MPa, NR = -207 dB) over shorter frequency ranges, while NANF A (with D = 100 μm) offers wider bands (61 MHz) and operation ranges (25 – 100 MHz). Our achievements are promising to overcome the ultrasound limitations faced by current optoacoustic sensors and transmitters. In addition, devices operating at frequencies considerably higher than 100 MHz are expected, providing unique possibilities to increase the spatial resolution to diagnose and treat microscale organisms in biomedical applications.

5. Methods

The selected NANFs are modelled by using the package COMSOL Multiphysics 6, based on FEM. The average dimensions of the fiber core and tube diameters D_C, D_T , and tube thickness T are estimated from experimental measures (NANF A: D_C = 33 μm, D_T = 26 μm, T = 745 nm; NANF B: D_C = 28 μm, D_T = 19 μm, T = 590 nm) [21]. The fibers cross section is designed as a 2D fiber geometry which is extruded along 1 mm to generate a 3D solid cylinder, using the methods described in [11,20]. The material is defined by the silica density ρ = 2200 kg/m^3, Young's modulus Y = 72.5 GPa and Poisson's ratio υ = 0.17 [11].

A constant sinusoidal force of $F = 3\times10^{-3}$ N is axially applied at the fiber end from f = 10 to 100 MHz (0.5 MHz step). F induces a pressure $P_0 = F/A_{eff}$ over the cross-section silica area A_{eff} representing the incident or generated ultrasound (e.g., from CNTs). A 100 μm thickness perfectly matched layer at the other fiber end works as an absorbing boundary condition, preventing reflections at the ending interface. Details about the 2D and 3D modeling are described in [11,20].

The induced pressure P, axial strain ε_z, and responsivity NR are evaluated in the silica tubes for distinct fiber diameters D (NANF A: D = 100, 125, 150, 162, 180 μm; NANF B: D = 80, 100, 125, 150, 162 μm). The maxima P and ε_z are evaluated by the software at the internal tubular edges forming the fiber core [23]. The ultrasound parameters are computed at each frequency step, and NR is analytically estimated using Equation (2) in Section 2. The simulations are performed by employing a high-performance computer cluster (HPC) (comprising 72 Intel® Xeon 3 GHz processor cores and memory of 960 GB).

Acknowledgements

This work was supported by the grants, #2022/10584-9, São Paulo Research Foundation (FAPESP), 305321/2023-4, 309989/2021-3 and 305024/2023-0, Conselho Nacional de Desenvolvimento Científico e Tecnológico (CNPq).

References

1. A. Taruttis and V. Ntziachristos, "Advances in real-time multispectral optoacoustic imaging and its applications," Nature Photonics **9**, 219–227 (2015).
2. A. Rosenthal, D. Razansky, D. Soliman, G. Wissmeyer, H. Estrada, M. Seeger, R. Shnaiderman, and V. Ntziachristos, "Fiber interferometer for hybrid optical and optoacoustic intravital microscopy," Optica 4, 10, 1180-1187 (2017).
3. Y. Jiang, H. J. Lee, L. Lan, H. Tseng, C. Yang, H. Y. Man, X. Han, and J. X. Cheng, "Optoacoustic brain stimulation at submillimeter spatial precision," Nature Communications 11, 1–9 (2020).

4. L. Shi, Y. Jiang, F. R. Fernandez, G. Chen, L. Lan, H. Y. Man, J. A. White, J. X. Cheng, and C. Yang, "Non-genetic photoacoustic stimulation of single neurons by a tapered fiber optoacoustic emitter," Light: Science & Applications 10, 1–13 (2021).
5. L. Shi, Y. Jiang, N. Zheng, J.-X. Cheng, and C. Yang, "High-precision neural stimulation through optoacoustic emitters," Neurophotonics 9, 032207 (2022).
6. T. Berer, I. A. Veres, H. Grün, J. Bauer-Marschallinger, K. Felbermayer, and P. Burgholzer, "Characterization of broadband fiber optic line detectors for photoacoustic tomography," J Biophotonics 5, 518–528 (2012).
7. I. A. Veres, P. Burgholzer, T. Berer, A. Rosenthal, G. Wissmeyer, and V. Ntziachristos, "Characterization of the spatio-temporal response of optical fiber sensors to incident spherical waves," J Acoust Soc Am 135, 1853 (2014).
8. S. Noimark, R. J. Colchester, B. J. Blackburn, E. Z. Zhang, E. J. Alles, S. Ourselin, P. C. Beard, I. Papakonstantinou, I. P. Parkin, and A. E. Desjardins, "Carbon-nanotube–PDMS composite coatings on optical fibers for all-optical ultrasound imaging," Adv Funct Mater 26, 8390–8396 (2016).
9. T. Berer, I. A. Veres, H. Grün, J. Bauer-Marschallinger, K. Felbermayer, and P. Burgholzer, "Characterization of broadband fiber optic line detectors for photoacoustic tomography," J Biophotonics 5, 518–528 (2012).
10. I. A. Veres, P. Burgholzer, T. Berer, A. Rosenthal, G. Wissmeyer, and V. Ntziachristos, "Characterization of the spatio-temporal response of optical fiber sensors to incident spherical waves," J Acoust Soc Am 135, 1853 (2014).
11. R. E. Silva and D. J. Webb, "Detailed spatial-spectral numerical characterization of axially symmetric broadband ultrasonic resonances in standard optical fibers," Optical Fiber Technology 75, 103192 (2023).
12. I. A. Veres, G. Flockhart, G. Pierce, B. Culshaw, T. Berer, H. Grün, P. Burgholzer, and B. Reitinger, "Numerical and analytical modeling of optical fibers for ultrasound detection," IEEE International Ultrasonics Symposium, IUS 520–523 (2011).
13. J. Dorighi, S. Krishnaswamy, and J. D. Achenbach, "Response of an embedded fiber optic ultrasound sensor," J Acoust Soc Am 101, 257 (1998).
14. A. Abdallah, C. Zhang, and Z. Zhong, "Phase sensitivity to acoustic pressure of microstrustured optical fibers: A comparison Study," International Journal of Signal Processing, Image Processing and Pattern Recognition 8, 105–114 (2015).
15. M. Pang, W. Jin, J. H. Cole, R. L. Johnson, P. G. Bhuta, J. A. Bucaro, and H. D. Dardy, "Detection of acoustic pressure with hollow-core photonic bandgap fiber," Optics Express 17, 11088–11097 (2009).
16. A. Abdallah, Z. Chaozhu, and Z. Zhi, "Investigation on the effect of underwater acoustic pressure on the fundamental mode of hollow-core photonic bandgap fibers," Int J Opt (2015).
17. A. Abdallah, C. Z. Zhang, and Z. Zhong, "Acoustic Pressure Sensing with Hollow-Core Photonic Bandgap Fibers," Applied Mechanics and Materials 738, 61–64 (2015).
18. R. E. Silva and D. J. Webb, "Ultra-efficient in-core acoustic waves in suspended core fiber for high frequency fiber-optic ultrasonic devices," Applied Physics Express 14, 087003 (2021).
19. R. E. Silva, J. H. Osório, G. L. Rodrigues, D. J. Webb, F. Gérôme, F. Benabid, C. M. B. Cordeiro, and M. A. R. Franco, "All-fiber broadband spectral acousto-optic modulation of a tubular-lattice hollow-core optical fiber," Optics Letters 49, 690-693 (2024).
20. R. E. Silva, J. H. Osório, G. L. Rodrigues, D. J. Webb, F. Gérôme, F. Benabid, C. M. B. Cordeiro, and M. A. R. Franco, "Highly efficient interaction of a tubular-lattice hollow-core fiber and flexural acoustic waves: design, characterization and analysis," arXiv:2402.15825 (2024).
21. H. Sakr, Y. Chen, G. T. Jasion, T. D. Bradley, J. R. Hayes, H. C. H. Mulvad, I. A. Davidson, E. Numkam Fokoua, and F. Poletti, "Hollow core optical fibres with comparable attenuation to silica fibres between 600 and 1100 nm," Nature Communications 11, 1–10 (2020).
22. G. Wissmeyer, M. A. Pleitez, A. Rosenthal, and V. Ntziachristos, "Looking at sound: optoacoustics with all-optical ultrasound detection," Light: Science & Applications **7**, 1–16 (2018).
23. Y. Cao, W. Jin, F. Yang, and H. Lut Ho, "Phase sensitivity of fundamental mode of hollow-core photonic bandgap fiber to internal gas pressure," Optics Express 22, 13190–13201 (2014).